Supporting Information

Influence of Mg the Li ion mobility in $Li_{4-2x}Mg_xP_2S_6$

Sven Neuberger[1], Neeshma Mathew[1], Sheyi Clement Adediwura[1], Jörn Schmedt auf der Günne*[1]

[1]University of Siegen, Faculty IV: School of Science and Technology, Department of Chemistry and Biology, Inorganic materials chemistry and Center of Micro- and Nanochemistry and Engineering (Cμ), Adolf-Reichwein-Straße 2, 57068 Siegen, Germany

*Corresponding author: gunnej@chemie.uni-siegen.de

Content

Figure S1: ^{31}P MAS NMR spectra over a wider ppm range

Figure S2: ^{31}P NMR T_1 relaxation.

Figure S3: Visualization of the structural transformation

Figure S4: Lattice parameters from Pawley fits of the X-ray powder diffractograms.

Figure S5: Activation energy from temperature dependent impedance spectroscopy measurements.

Figure S6: Equivalent circuit model used for fitting the impedance measurements and the corresponding Nyquist plot of $Li_{3.74}Mg_{0.13}P_2S_6$ showing the experimental data and fit quality.

Figure S7: Results from nudged elastic band calculations for an Mg dopant hopping onto a neighboring vacancy site.

Figure S8: Results from nudged elastic band calculations for a vacancy hopping motion onto neighboring Li sites for a motion along *c*-axis.

Figure S9: Results from nudged elastic band calculations for a vacancy hopping motion onto neighboring Li sites for a motion along *a*-axis.

Figure S10: Scanning electron microscopic image of $Li_4P_2S_6$.

Figure S11: Scanning electron microscopic image of $Li_{3.74}Mg_{0.13}P_2S_6$.

Figure S12: Scanning electron microscopic image and electron dispersive X-ray analysis data of $Li_4P_2S_6$.

Figure S13: Scanning electron microscopic image and electron dispersive X-ray analysis data of $Li_{3.74}Mg_{0.13}P_2S_6$.

^{31}P MAS NMR spectra over a wide ppm range
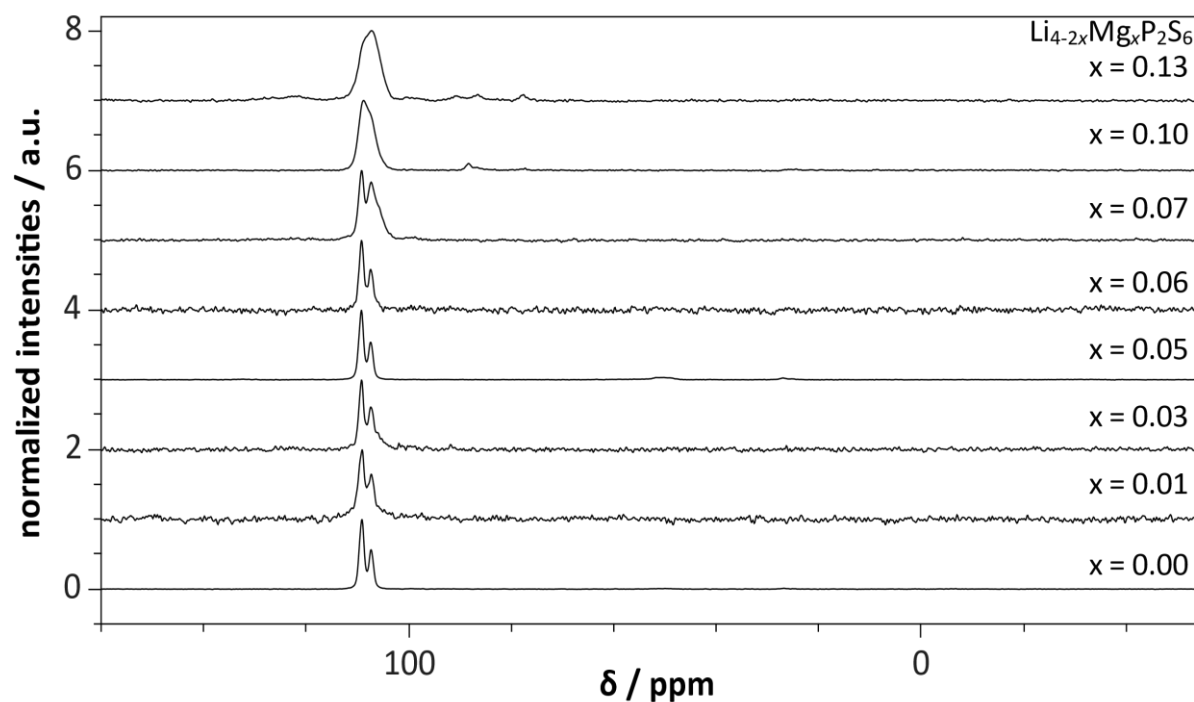
Figure S1: Experimental ^{31}P MAS NMR spectra of $Li_{4-2x}Mg_xP_2S_6$ at sample spinning frequency v_{rot} of 10 kHz shown at a range from –50 to 150 ppm. At low Mg content, the ^{31}P MAS NMR spectra contain the characteristic signals of $Li_4P_2S_6$ with a peak area ratio of exactly 1.0:2.0, which merge to one broad signal at Mg concentrations at $x > 0.06$. There are no additional ^{31}P NMR signals in the range between 0 to –30 ppm, which are significant for oxygen containing phases.

^{31}P NMR T_1 Relaxation

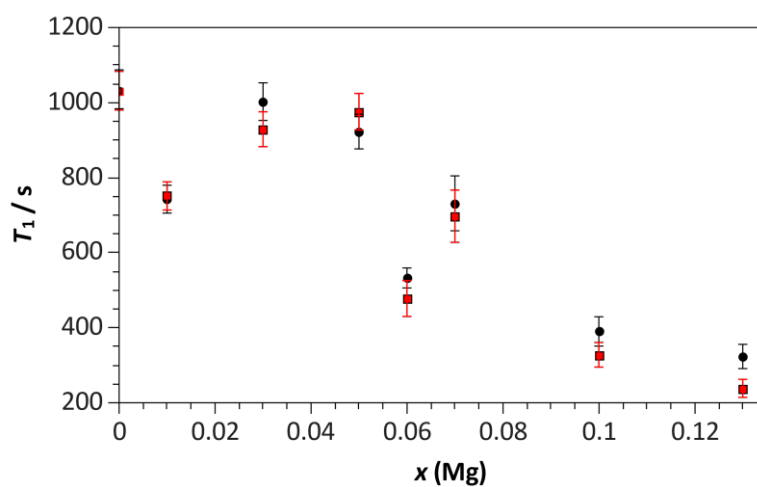

Figure S2: T_1 relaxation times of both ^{31}P NMR signals (the signal at 109.2 ppm corresponds to black dots and the signal at 107.2 ppm to red squares) of $Li_{4-2x}Mg_xP_2S_6$ at 121.50 MHz. The T_1 relaxation times of both signals decrease with increasing Mg^{2+} concentration.
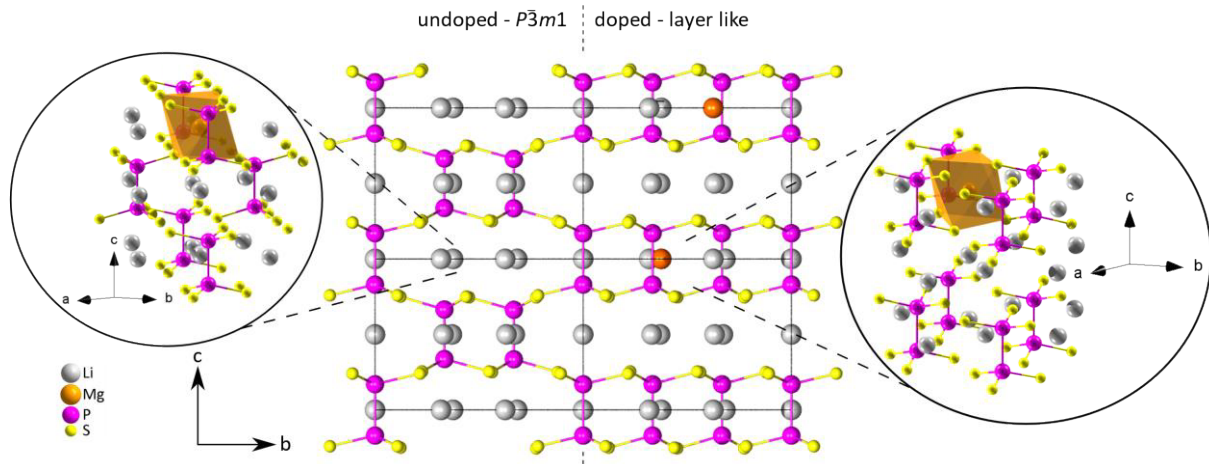
Visualization of the structural transformation

Figure S3: Visualization of a 2x2x2 supercell of $Li_{4-2x}Mg_xP_2S_6$. The structural transformation from space group $P321$ (left cells) to a layered structural model occurs due to an incorporation of Mg^{2+} ions. The doping process leads to a $P31m$ like layered alignment of the $P_2S_6^{4-}$ units similar as for $Mg_2P_2S_6$ (space group $C2/m$) and as expected for the structural model of $Li_{3.33}Mg_{0.33}P_2S_6$ (space group $P31m$)[26]. The insets show the coordination environments for the Mg^{2+} ions (orange) for the different structural models. In space group $P321$, the coordination polyhedra of Mg^{2+} are slightly distorted due to a different alignment and thus a different number of $P_2S_6^{4-}$ units surrounding the central atom of the polyhedron.
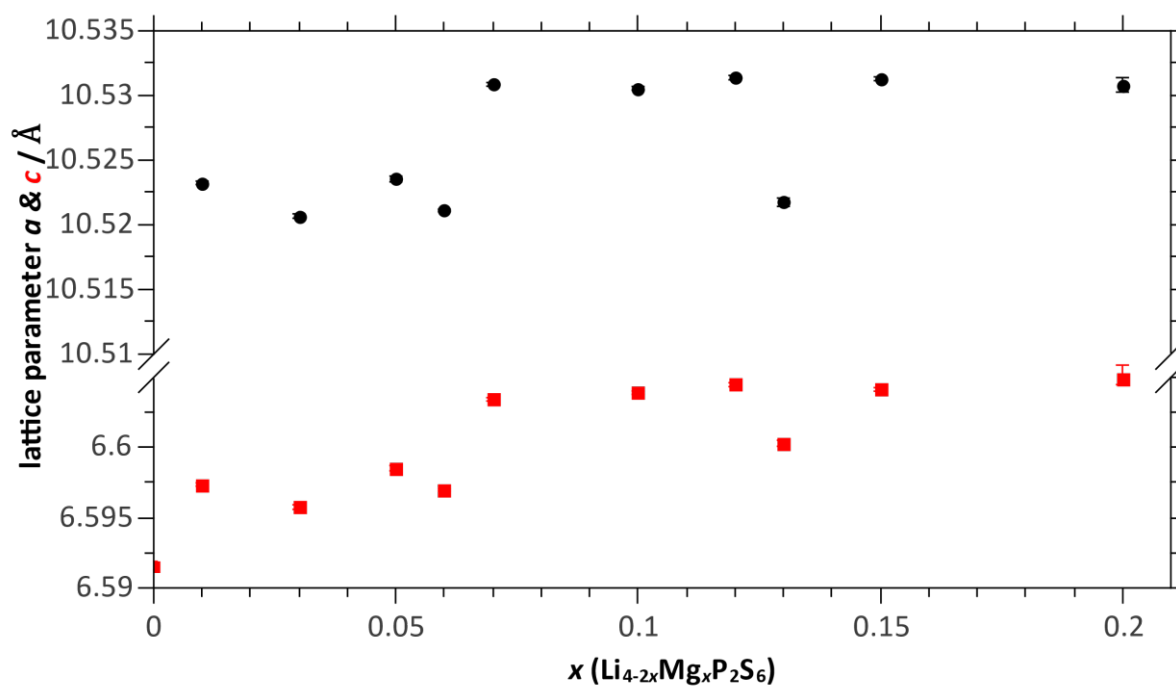
Results of the Pawley fits

Figure S4: Plot of the lattice parameters *a* (black) and *c* (blue) in dependence of the Mg^{2+} content *x* in $Li_{4-2x}Mg_xP_2S_6$ after determined by a Pawley fit of the XRD data. With increasing Mg^{2+} content, all lattice parameters increase and show a convergent behavior at concentrations of $x \geq 0.07$.

Impedance spectroscopy

An equivalent circuit (Fig. S5a) was used in fitting fit the EIS data (Fig. 5b). The ionic conductivity was estimated according to equation S5[1].
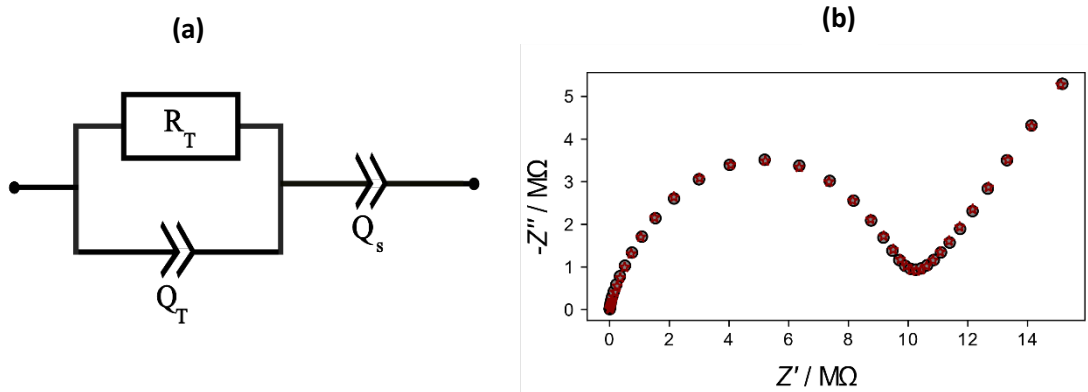
(a) **(b)**

Figure S5: (a) Equivalent circuit consisting of a resistance R_T and a constant phase element Q_T depicting the overall impedance of the sample and a constant phase element Q_S for the electrode region. (b) The plot of imaginary part against real part of the measured impedance of $Li_{3.74}Mg_{0.13}P_2S_6$ pellet (diameter = 13 mm, thickness = 1 mm) at 363 K. The grey cycles represent the experimental data while red asterisks represent the fit obtained from the equivalent circuit.

The ionic conductivity is given as [1]:

$$\sigma = \frac{l}{R\,A} \tag{S5}$$

Here, A is the cross-sectional area and l is the thickness of the sample.

C_{eff} is calculated using equation S6[2,3].

$$C_{eff} = (Q \cdot R^{(1-\alpha)})^{1/\alpha} \tag{S6}$$

Here, C_{eff} is the effective capacitance, Q is the constant phase element, R is the resistance and α is the exponential factor of the constant phase element.

The activation energy for the macroscopic ion conductivity is estimated using the Arrhenius law[4] (equation S7).

$$\sigma = \sigma_0 \exp\left(-\frac{E_A}{k_B T}\right) \tag{S7}$$

Here, σ_0 is the conductivity at infinite temperature, E_A the activation energy, k_B Boltzmann's constant, and T the temperature. The natural logarithmic of equation S7 can be used to fit the experimental data (Figure S6).

$$\ln \sigma \; (\text{S/cm}) = -\frac{E_A}{k_B}\left(\frac{1}{T}\right) + \ln \sigma_0 \left(\frac{\text{S}}{\text{cm}}\right) \tag{S8}$$
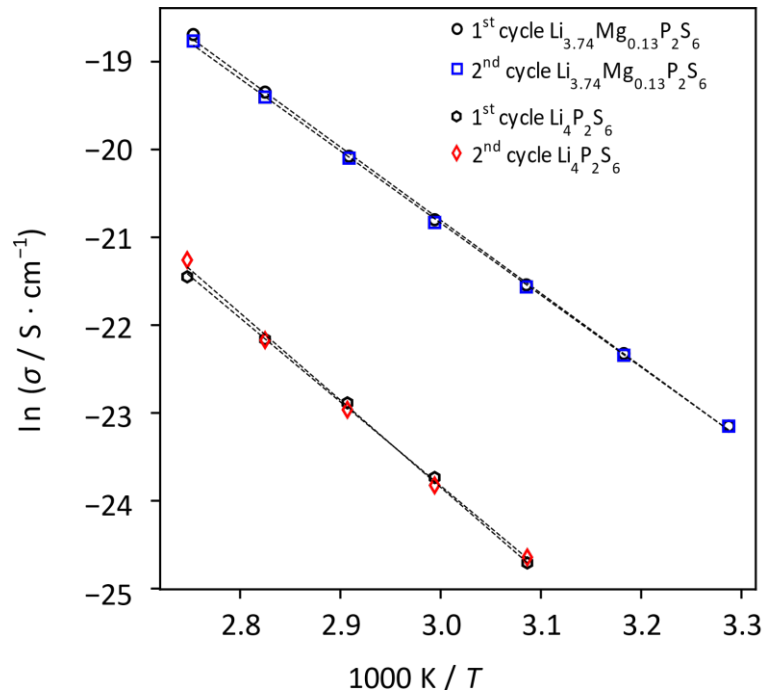
Figure S6: Arrhenius plot of the logarithmic ion conductivities of $Li_4P_2S_6$ and $Li_{3.74}Mg_{0.13}P_2S_6$ as a function of the reciprocal temperature for both heating cycles and the linear fits indicated by dashed lines. The activation energy for the macroscopic Li ion motion can be estimated from the slope of a linear fit.
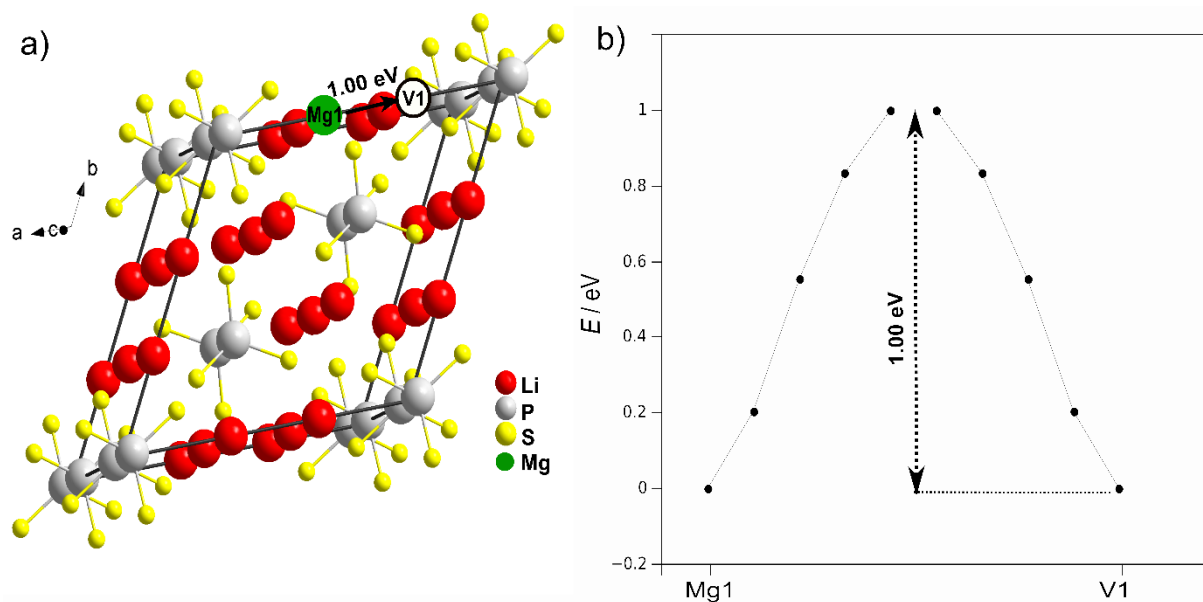
Nudged Elastic Band Calculations

Figure S7: Probable pathways of vacancy mediated Mg-ion migration and the associated activation energies calculated using nudged elastic band calculations by creating a vacancy (V1) in the structure by adding Mg^{2+} (Mg1) ion by replacing Li^+ ion. a) Mg-ion migration path from Mg1 to V1 (vacancy-1) in the ab-plane within the structure $Li_4P_2S_6$ (space group $P321$). The arrow represents the transport of Mg-ion from one to the other site which is vacant (V1). b) The graph shows the energy barrier for the Mg-ion jump from Mg1 to the nearest vacancy site V1.
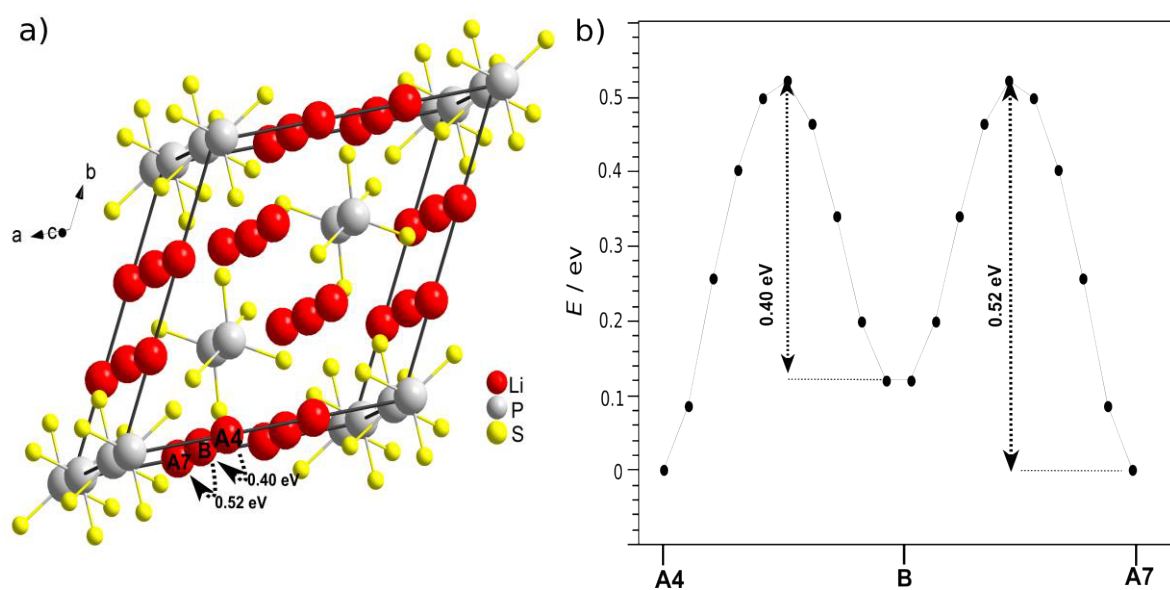

Figure S8: The activation energy barrier calculated for $Li_4P_2S_6$ using nudged elastic band calculations through vacancy mediated diffusion from A4 to B. a) The long range Li-ion transport from site A4→B→A7 along the c-axis for $Li_4P_2S_6$. The dashed lines show the activation energy from site A4→B and B→A7 for the entire unit cell of the compound $Li_4P_2S_6$. b) The activation energy barrier for the pathways from A4→B→A7 along the c-axis.
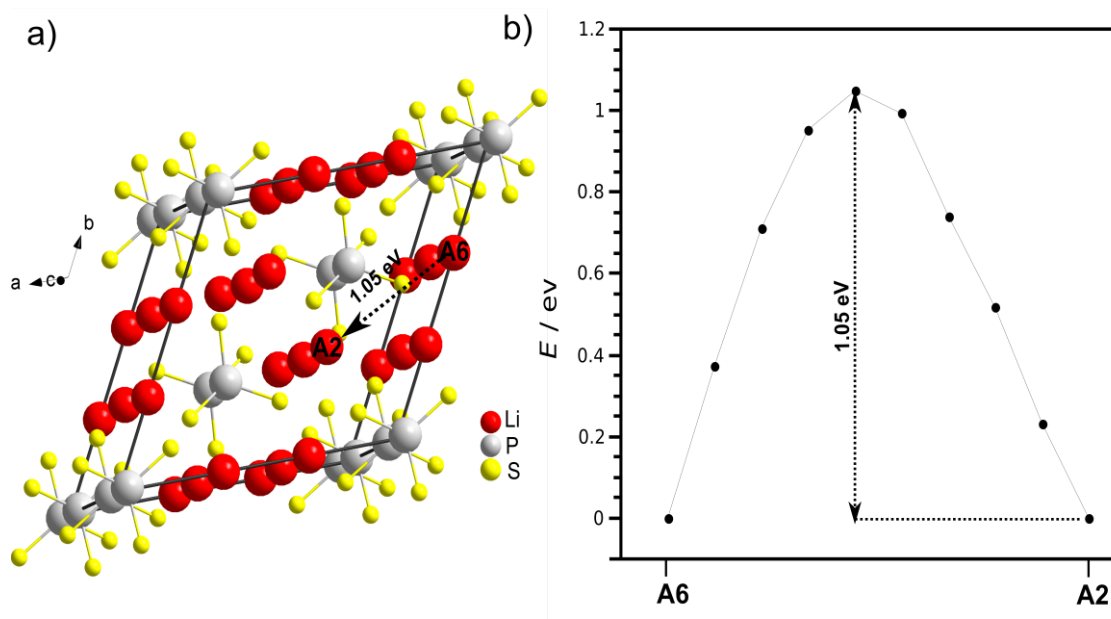
Figure S9: The activation energy barrier calculated for $Li_4P_2S_6$ using nudged elastic band calculations by vacancy mediated diffusion from A6 to A2. a) The short range Li-ion transport from site A6 to A2 for $Li_4P_2S_6$. The dashed line shows the vacancy mediated diffusion pathway from A6 to A2. b) The activation energy barrier for the pathway from A6 to A2 along a-axis.

Scanning Electron Microscopy and Energy Dispersive X-Ray Analysis

Experimental part

Scanning electron microscopy (SEM) and electron dispersive X-ray (EDX, EDAX) analysis were carried out using CamScan 44, vintage 1991 (Siegen, Germany). Liquid nitrogen cooled Si (Li) X-ray EDS detector is attached to the SEM. All images were taken out at an acceleration voltage of 25 kV, aperture 50 μ with a working distance of 35 mm using either a secondary electron detector or back scattered electron detector. Scandium/ Olympus SIS and EDAX Genesis (Version 5) software were used for scanning electron microscopy and electron dispersive X-ray analysis, respectively.

The samples for measurement were prepared inside the glove box (MBraun, Garching, Germany) and transferred from glove box to instrument using a Schott glass to reduce contact with air.

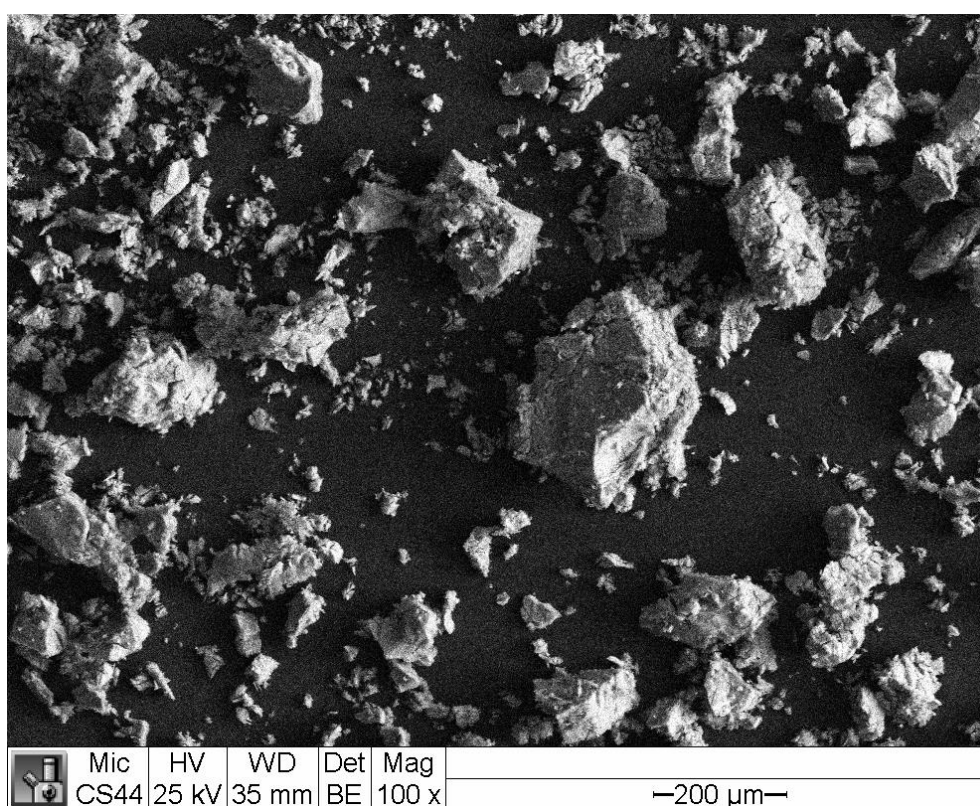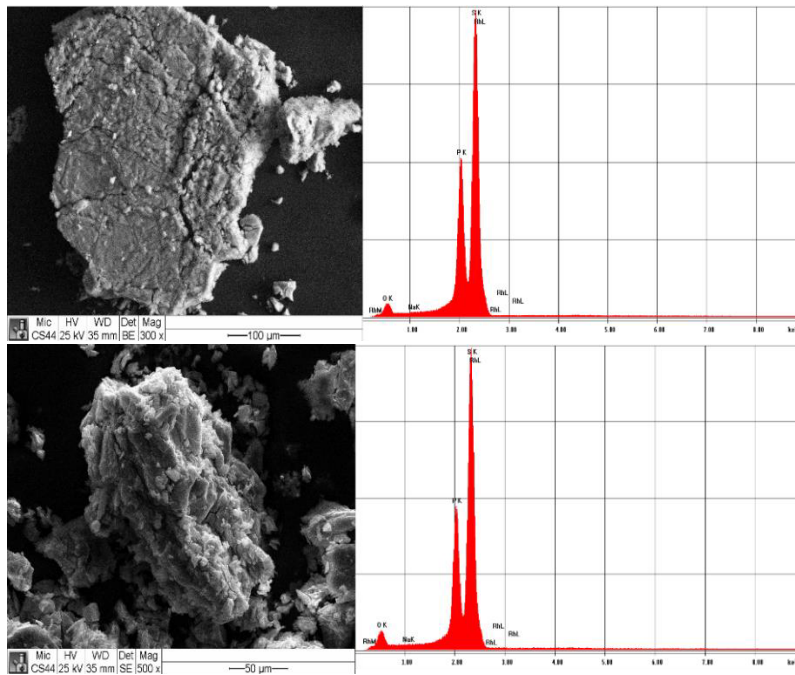## Scanning Electron Microscopy and Energy Dispersive X-Ray Analysis

Figure S10: Scanning electron microscopic image of $Li_4P_2S_6$. The back scattered image detector is used to produce the image and the image is 100 times magnified.

Figure S11: Scanning electron microscopic image of $Li_{3.74}Mg_{0.13}P_2S_6$. The back scattered image detector is used to produce the image and the image is 50 times magnified.
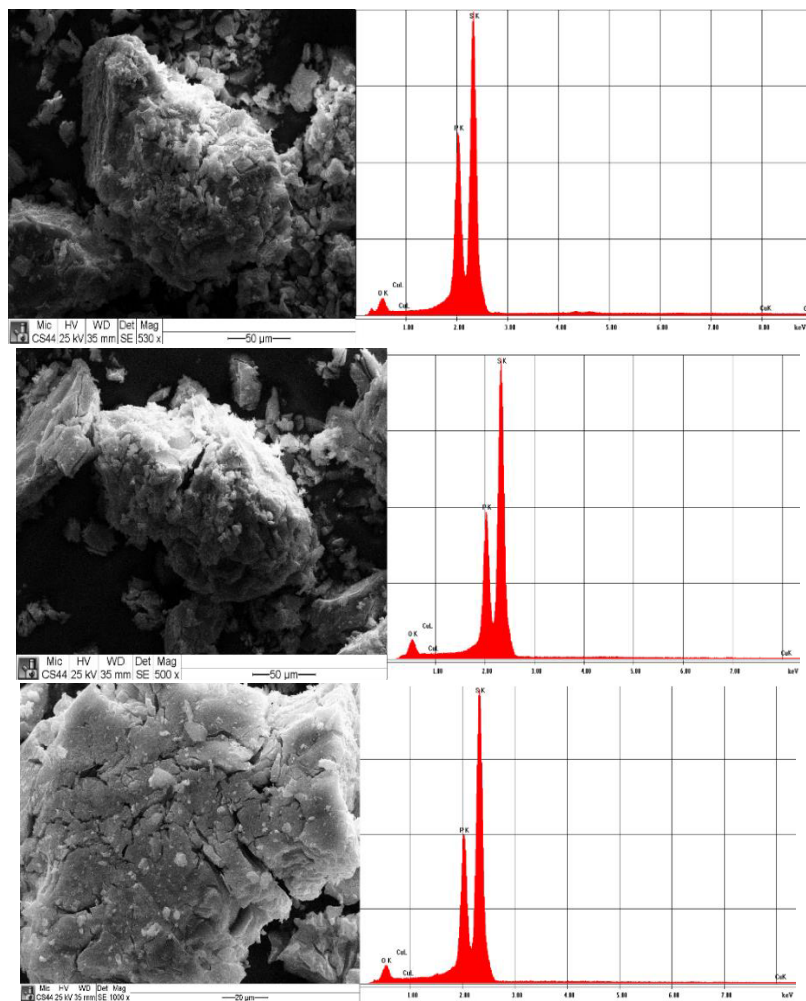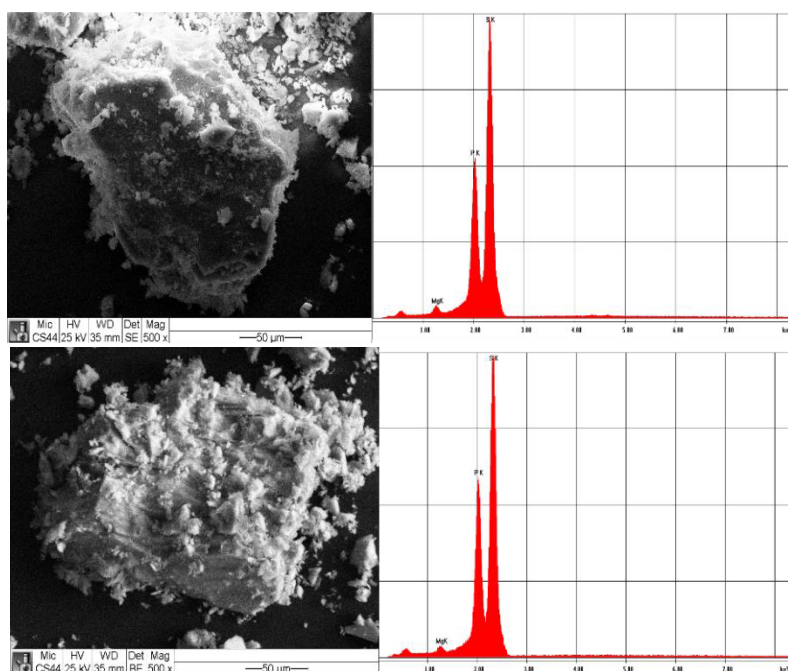
Figure S12: Scanning electron microscopic image of crystallites shown in figure S10 and electron dispersive X-ray analysis data on $Li_4P_2S_6$. The predominant components were found to be phosphorous and sulfur. The detector (det) used for the detection is shown in each figure as back scattered electrons (BE) or secondary electrons (SE). The magnification (Mag) power of individual figures are also shown in individual figures.

Figure S13: Scanning electron microscopic image and electron dispersive X-ray analysis data of $Li_{3.74}Mg_{0.13}P_2S_6$ of the crystallites shown in figure S11. The predominant components were found to be phosphorous, sulfur and magnesium. The detector (det) used for the detection is shown in each figure as back scattered electrons (BE) or secondary electrons (SE). The magnification (Mag) power of individual figures are also shown in individual figures.
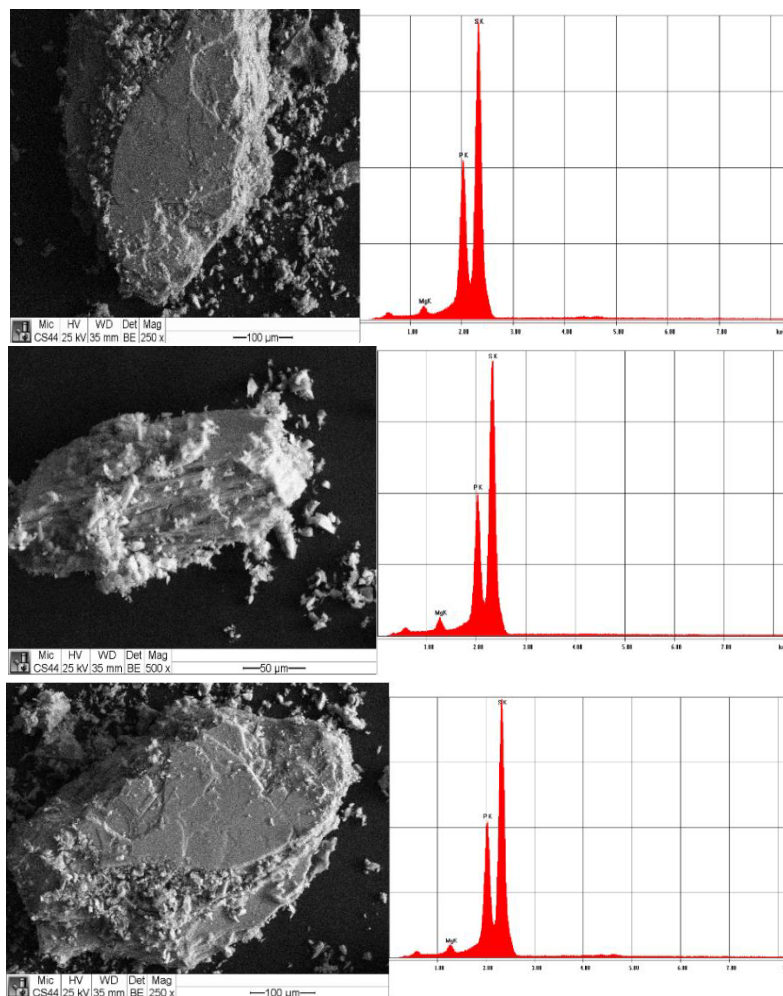
References

[1] E. Barsoukov, J. R. Macdonald, Eds., *Impedance Spectroscopy: Theory, Experiment, and Applications*, Wiley, Hoboken, NJ, **2018**.

[2] G. J. Brug, A. L. G. van den Eeden, M. Sluyters-Rehbach, J. H. Sluyters, *Journal of Electroanalytical Chemistry and Interfacial Electrochemistry* **1984**, *176*, 275–295.

[3] J. S. Lee, U. Anselmi-Tamburini, Z. A. Munir, S. Kim, *Electrochemical and Solid-State Letters* **2006**, *9*, J34.

[4] S. Lanfredi, A. C. M. Rodrigues, *Journal of Applied Physics* **1999**, *86*, 2215–2219.